Chemical Engineering Journal 466 (2023) 142708

Contents lists available at ScienceDirect

Chemical Engineering Journal

journal homepage: www.elsevier.com/locate/cej

Solar-driven calcium looping in fluidized beds for thermochemical energy storage

Claudio Tregambi [a,b], Francesca Di Lauro [c], Sara Pascual [d], Pilar Lisbona [d], Luis M. Romeo [d], Roberto Solimene [b,*], Piero Salatino [b,e], Fabio Montagnaro [c]

[a] Dipartimento di Ingegneria, Università degli Studi del Sannio, Piazza Roma 21, 82100 Benevento, Italy
[b] Istituto di Scienze e Tecnologie per l'Energia e la Mobilità Sostenibili, Consiglio Nazionale delle Ricerche, Piazzale Tecchio 80, 80125 Napoli, Italy
[c] Dipartimento di Scienze Chimiche, Università degli Studi di Napoli Federico II, Complesso Universitario di Monte Sant'Angelo, 80126 Napoli, Italy
[d] Departamento de Ingeniería Mecánica. Escuela de Ingeniería y Arquitectura (EINA). Universidad de Zaragoza, C/ María de Luna s/n, 50018 Zaragoza, Spain
[e] Dipartimento di Ingegneria Chimica, dei Materiali e della Produzione Industriale, Università degli Studi di Napoli Federico II, Piazzale Tecchio 80, 80125 Napoli, Italy

ARTICLE INFO

Keywords:
Concentrated solar thermal power
Calcium looping
Fluidized bed
Lime-sand interaction
Sorbent deactivation
Thermochemical energy storage

ABSTRACT

Integration between Concentrated Solar Power (CSP) and Calcium Looping (CaL) is gaining consideration in the perspective of large shares of renewable energy sources, to smooth the variability of non-dispatchable energy input. The scope of this study is to investigate the CaL process for ThermoChemical Energy Storage (TCES), by performing a dedicated experimental campaign in fluidized bed under realistic process conditions suitable for CaL-CSP integration. Chemical deactivation of the limestone-based sorbent has been assessed by measuring the extent of Ca carbonation along iterated calcination/carbonation cycles, correlated with physico-chemical characterization of the sorbent at selected stages of the conversion. Properties that have been scrutinized were particle size distribution, bulk density, and particle size, density, and porosity of bed solids. The attainable values of energy storage density were evaluated as well.

A remarkable finding of the experimental campaign is the pronounced synergistic deactivation of limestone when it is co-processed with silica sand. Chemical interaction of CaO with the silica sand constituents at the process temperatures has been scrutinized as possible responsible for the loss of reactive CaO toward CO_2 uptake. Post-process of particle density data, together with N_2-intrusion porosimetric analysis, and quantitative and qualitative XRD analyses, suggests that the sand/lime interaction induces a strong reduction of the total and reactive sorbent porosity and, in turn, of reactivity.

Density-based classification to separate converted and unconverted limestone particles after the carbonation step has been evaluated with the goal of increasing process efficiency, by avoiding the circulation of streams with unreacted particles through the plant. For this purpose, the minimum fluidization velocity of calcined and carbonated particles has been measured after each reaction step at the relevant process temperature.

1. Introduction

The ambitious targets of the European Green Deal aim to cut the greenhouse gas emissions by at least 55% within 2030, and to achieve carbon neutrality by 2050 with net-zero greenhouse gas emissions. These objectives require a strong decarbonization of the power and energy sectors, with an ever-increasing exploitation of renewable energy sources. Among them, solar energy is bound to play a key role in the future economy because of its virtual unlimited potential and wide availability. However, a strategy to deal with its intermittent nature needs to be implemented to enable its massive deployment.

Concentrated Solar Power (CSP) technologies provide an effective path for exploitation of solar energy, allowing integration with thermal and thermochemical energy storage systems to overcome its intrinsic intermittency. In CSP systems, a field of heliostats (i.e., sun tracking mirrors) is used to focus and concentrate the solar energy onto a receiver. Here, a heat transfer medium is heated at moderate–to–high temperatures and eventually used to sustain energy intensive chemical/physical processes, or to drive thermodynamic cycles for energy generation. Most recent commercial CSP plants make use of molten salts (i.

* Corresponding author.
E-mail address: roberto.solimene@cnr.it (R. Solimene).

https://doi.org/10.1016/j.cej.2023.142708
Received 11 October 2022; Received in revised form 20 March 2023; Accepted 29 March 2023
Available online 31 March 2023

e., a binary mixture of $NaNO_3$ and KNO_3) as heat transfer medium, which operate within the 290–565 °C temperature range. Storage of the hot medium in insulated vessels, rather than direct use (i.e., thermal energy storage), allows decoupling the two steps of solar energy collection and exploitation, enhancing the dispatchability of solar energy. Research efforts on the CSP technology are mostly prioritized on: i) increasing the maximum working temperature of the heat transfer medium, currently limited at 565 °C due to the molten salts degradation; ii) developing more efficient energy storage systems with respect to storage density, application temperature, and time scale of utilization. On one side, particle receivers are under the spotlight to overcome the temperature limitations of the molten salts: dense-solids suspensions can indeed safely work at temperatures of 1000 °C and over [1–3]. On the other side, use of reversible chemical reactions to store solar energy in the form of chemical bonds (i.e., ThermoChemical Energy Storage, TCES) is widely pursued [4–7]. Gas-solid chemical reactions are the most investigated. Indeed, their higher reaction enthalpy turns into potential higher values of energy storage densities and the easier separation of the reaction products favours the subsequent storage/transportation.

Particle receivers able to simultaneously work as solar receiver and chemical reactor can represent a breakthrough for the success of the CSP–TCES technology. For this reason, Fluidized Bed (FB) systems have been and are widely investigated [8–10]. Literature research studies spread from conventional FB with direct/indirect irradiation [11–13], to innovative design targeted at: i) increasing the axial thermal diffusivity by internal circulation [14–16], spout, pulsed or uneven fluidization [2,17–20]; ii) providing a more uniform residence time distribution by multistage operation [21–23]; iii) exploiting the sensible heat of the reaction products for the heating of the reactants by internal solid–solid heat exchangers [2,24,25].

The selection of the most appropriate chemical reaction for TCES is open to debate. Apart from solar fuels production, decomposition and recombination of metal hydroxides, carbonates, oxides and perovskites are among the most investigated processes, each with specific advantages and drawbacks [26–29]. In particular, reversible calcination-carbonation of Ca–based sorbents, Eq. (R_1):

$$CaCO_3 \leftrightarrows CaO + CO_2 \quad (R1)$$

has been widely addressed recently, and its integration with CSP is being currently assessed, with different European research projects currently active [30,31].

The same reaction scheme has been widely investigated in literature for post combustion and atmospheric CO_2 capture, and is commonly referred to as Calcium Looping (CaL) [32–35]. CSP–CaL integrated processes targets both CO_2 capture [34,36,37] and TCES. The interest on this system for TCES applications mainly springs from: i) the fairly high reaction enthalpy of the chemical reaction ($|\Delta H_r^\circ|_{298K} = 178$ kJ mol^{-1}); ii) the high temperature at which solar energy can be retrieved (650–850 °C according to the process parameters), which allows integration with high-efficiency Rankine/Brayton cycles [38]; iii) the low cost of the raw material (i.e., limestone, a very cheap natural sorbent rich in $CaCO_3$). On the other side, the major weakness of the CaL cycle is the decay of material reactivity over iterated cycling, induced by loss of porosity (i.e., thermal/chemical sintering) and pore plugging [39–41]. Different techniques have been explored to prevent or limit the loss of reactivity, among which: production of composite materials with inert stabilizers/promoters [42] such as ZrO_2 [43–45], Al_2O_3 [46,47], CeO_2 or multiple Ce/Al/Zr additives [48], eutectic alkali chloride salts [49]; mechanical activation [50,51]; thermal pre-treatments [52,53]; use of steam [54–56]. More recently, introduction of inert materials in synthetic Ca–based sorbents has been scrutinized also with the aim of improving their optical performance in terms of solar energy absorptivity, through the synthesis of particles characterized by a darker colour [57–59]. On this topic, a peculiar natural sorbent with a higher absorption of solar energy has also been tested with positive outcomes [60]. While improving material stability, it was recently found that the presence of inert compounds does not significantly affect the kinetics of carbonation, and a slight modification of the parameters of the random pore model may be sufficient to account for the presence of inert stabilizers [61]. Different process schemes have been proposed and investigated in literature for integration between CSP and CaL for TCES. Tregambi et al. [41] distinguished between open loop and closed loop conditions with respect to CO_2. In the open loop condition, CaO carbonation is performed at 650 °C using a stream coming from a CO_2 emitting industry, whereas calcination is performed at 850 °C using air, and the produced stream is released to the atmosphere. Differently, in closed loop conditions, calcination is performed at 940–950 °C under CO_2, that can then be recycled to the process. Experimental tests performed in a FB heated by a solar simulator demonstrated that the harsher conditions of closed loop during calcination induce a stronger loss of reactivity [41]. Castilla et al. [62] investigated a process scheme for simultaneous TCES and CO_2 capture, and performed a techno-economic analysis of the system. Sarrión et al. [63,64] proposed, instead, two different process configurations for a closed loop CO_2 cycle for TCES. In both schemes, carbonation is carried out at 850 °C under pure CO_2, to maximize the efficiency of the subsequent cycle for energy production. Calcination is instead performed either at 750 °C under a N_2/He atmosphere [63,64], or at 950 °C under pure CO_2 [64]. In the former case, use of membranes is proposed to separate the produced CO_2 from the carrier gas and close the looping cycle. Experimental tests have been performed only in a thermogravimetric analyzer, but proved again that harsher conditions during calcination promote material sintering. The closed loop CO_2 scheme, with carbonation/calcination at 850/950 °C under pure CO_2, has been investigated by model computations also by Pascual et al. [65], who proposed the addition of a solid–solid separation unit after the carbonator to separate converted and unconverted particles, thus avoiding the looping of unreacted streams, to increase process efficiency. Since CaO carbonation to yield $CaCO_3$ is generally proved to be a slow reaction step because of the time required for internal CO_2 diffusion [61], it is reasonable to consider that unconverted streams may leave the carbonator during continuous operation, thus supporting the usefulness/advantages of a Solid-Solid Separation Unit (SSU). The feasibility of this operation is, however, still to be demonstrated.

The aim of this study is to contribute to the existing knowledge on the CaL process for TCES, by performing a dedicated experimental campaign under realistic process conditions suitable for CaL-CSP integration, which are different from those typically investigated in literature for carbon capture and storage. The closed loop CO_2 scheme, considering carbonation/calcination at 850/950 °C under pure CO_2, has been selected because of its interesting features and because of the lack of experimental data in apparatus different from thermogravimetric analyzers. In this work, experimental tests were performed in FB reactors because of their peculiarity of acting, simultaneously, as particle receivers for solar radiation and multiphase chemical reactors. Decay of material reactivity and deactivation trend, as well as changes in granulometric distribution of the bed inventory over cycling, were deeply scrutinized. Attainable values of energy storage density were also computed. Moreover, the aim of increasing the overall process efficiency of the process has been pursued by avoiding the circulation of unreacted streams [65]. To this end, it was evaluated the possibility of separating converted (i.e., $CaCO_3$-based) and unconverted (i.e., CaO-based) particles after the carbonation step, exploiting the particle density difference. For the purpose, the minimum fluidization velocity of calcined and carbonated particles was experimentally measured after each reaction step at the relevant process temperature, to gather first data about the feasibility of this operation. Finally, the influence of silica sand on the CaL performance, when experiments were carried out using sand as ballast bed material, was highlighted.

2. Process scheme

The process plant devised for the closed loop CaL cycle for TCES is sketched in Fig. 1. The system entails two fluidized bed reactors (i.e., a solar calciner and a carbonator), three intermediate Storage Tanks (STs) required to decouple collection and exploitation of solar energy (i.e., one each for the calcined and carbonated material, one for the compressed CO_2), a SSU at the exit of the carbonator, and several Heat Exchangers (HEs) for heat recovery or preheating. A heat loss of 2% was assumed for each heat exchanger used for heat recovery. Operation of the process is described in the following. More extent information of the theoretical simulation of the CaL process as TCES is detailed by Pascual et al. [66]. A stream of carbonated material (consisting of partially carbonated particles because of uncomplete carbonation [41]) is fed from either the ST1 $CaCO_3$ storage tank (upon preheating from 200 to 850 °C through HE1) or from the carbonator itself to the calciner. Here, endothermic calcination occurs driven by concentrated solar energy (100 MW energy input as reference case). Gaseous atmosphere is 100% CO_2, therefore a process temperature of about 950 °C is required to guarantee fast reaction kinetics. The stream of pure CO_2 exiting the reactor is partially recycled as fluidizing gas to the reactor, and partially either sent to compression and ST3 (upon heat recovery from 950 °C to 50 °C in HE3) or directly fed to the carbonator. The CO_2 is stored in ST3 at 75 bar and 35 °C, after being previously compressed and cooled in 4 interleaved stages (CCT in Fig. 1). A pressure ratio of 3 was assumed for each of the four compression stages to finally reach the CO_2 storage pressure (75 bar). The energy penalty associated to the compression stages is the electrical energy consumption, rising to 8.41 MW maximum [66]. The first three cooled stages reduce the temperature to 50 °C and the fourth to the CO_2 storage temperature (35 °C). The heat from the cooled stages is recovered, being the heat losses of 2%. Similarly, particles leaving the calciner are sent to ST2 (upon heat recovery from 950 °C to 200 °C in HE6), or directly to the carbonator. Finally, the calciner also processes an additional stream of fresh limestone and purges a stream of spent material, which is required to compensate for the decay of material reactivity over cycling ("chemical loss") and for the elutriation of fine particles generated upon attrition/fragmentation phenomena ("physical loss") [67,68]. The fresh limestone is fed at ambient temperature (25 °C) and a heat recovery of the purged spent material is done through HE8 from 950 °C to 200 °C. The calcination step is in operation only upon availability of solar energy (ECL). When the collected solar energy needs to be retrieved (ECR), CaO and CO_2 are fed to the carbonator either from the CaO/CO_2 storage tanks (ST2 and ST3) (upon preheating through HE7 and HE5, respectively) or directly from the calciner. The HE7 receives CaO streams from (i) calciner at 950 °C and (ii) ST2 at 200 °C to be preheated to carbonator conditions (850 °C). The HE5 preheats the CO_2 mixture from ST3 at 15 °C and calciner at 950 °C to 850 °C. The CO_2 from ST3 suffers a discharging expansion (DE in Fig. 1) before being fed into HE5 at 15 °C. Reactive atmosphere in the carbonator is 100% CO_2: carbonation is then performed at high temperature (850 °C) to maximize the efficiency of the subsequent thermodynamic cycle for power production. The carbonation reaction is generally a slow reaction step because of the time required for internal CO_2 diffusion. Fluidized beds may be viewed as continuously stirred tank reactors in terms of solid residence time distribution. Thus, it is reasonably to consider that the solid stream exiting the carbonator includes both carbonated particles (consisting of both CaO and $CaCO_3$, mostly concentrated in the core and shell of the particle, respectively) and unreacted (or less carbonated) particles. Unreacted CO_2 stream is found at carbonator outlet given the uncomplete exothermic carbonation reaction. The unreacted CO_2 from carbonator is sent to the CCT after a heat recovery from 850 °C to 50 °C in HE4. The carbonator model applied for the theoretical CaL TCES simulation was based on the kinetic model described by Grasa et al. [69] under carbon capture conditions (650 °C and 10–15 $\%_v$ of CO_2). A SSU is then implemented for the separation of carbonated and unreacted particles: carbonated material is sent either to ST1 (upon heat recovery from 850 °C to 200 °C in HE2) or to the calciner, whereas unreacted or less reacted material is cycled back to the carbonator at 850 °C, closing the looping cycle. To allow the solid–solid separation, the SSU consists of a tapered fluidized bed reactor operated under transient fluidization regime, so as to induce segregation of lower density particles to the top of the column [70,71]. The inclusion of the total separation of carbonated and unreacted particles was firstly proposed by Pascual et al. [65] to enhance the energy efficiency of the CaL TCES system. Moreover, the effect of the SSU on the energy penalties and plant size reduction was assessed under theoretical simulation. The threshold scenarios (no separation and total separation of solids after carbonation step) were evaluated to provide information of the maximum and minimum energy and size requirements. A size reduction between 53 and 74 % was showed for heat exchangers affected by solid streams when the SSU is included [66].

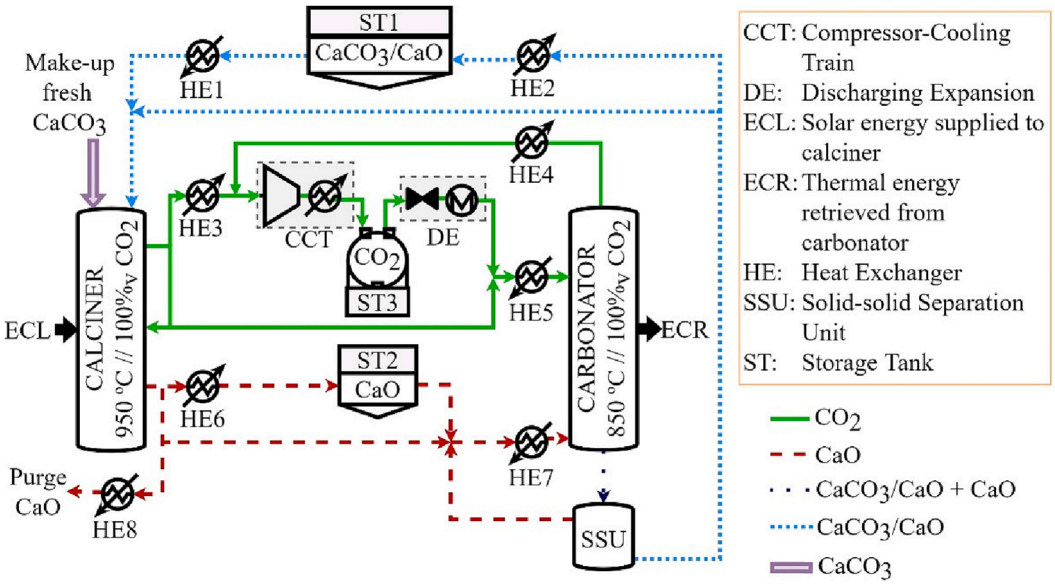

Fig. 1. Simplified conceptual scheme for closed loop CaL-CSP integration, taken as reference in this work.

3. Experimental

The experimental campaign consisted in CaL tests performed under operating parameters relevant for the process integration outlined in the previous paragraph. Tests were performed in semi–batch mode using a single FB reactor, by switching the process conditions between carbonation and calcination. Two different experimental rigs were used for the whole experimental campaign: i) a fluidized bed reactor equipped with a solar simulator, to mimic the effect of concentrated solar radiation and estimate the decay of reactivity over cycling; ii) an electrically heated fluidized bed reactor, to determine the changes in the particle properties (granulometric distribution, porosity and density) of the bed inventory over cycling, as well as the minimum fluidization velocity of the material after each reaction step.

3.1. Experimental apparatus

The FB reactor used for the CaL tests under solar simulated conditions is sketched in Fig. 2. The reactor has been used in previous experimental campaigns and a comprehensive description of the experimental rig can be found in [41,52]. The FB reactor has an internal diameter of 0.1 m and, starting from the bottom, is made of three components: i) a windbox with an upper perforated plate serving as gas distributor (0.5 mm holes on a triangular pitch); ii) a fluidized bed section, 0.1 m high; iii) a conical freeboard section (0.4 m high, internal cone angle of about 30°) with an upper optical window required to seal the reactor environment while allowing entrance of the concentrated solar radiation. At middle height of the conical section, four discharge ports (1 in. diameter) are provided for gas outlet. The reactor is heated by: i) a gas heater (manually controlled), able to heat the gaseous stream up to 700 °C; ii) two semicylindrical radiant heaters (driven by a PID controller) which surround the windbox and fluidized bed sections; iii) a solar simulator, made up by three 4 kW_e short–arc Xe–lamps coupled with elliptical reflectors, able to produce a peak flux of about 3 MW m^{-2} and a total irradiated power of about 3.2 kW_{th} on the bed surface. Electronic mass flow controllers are used for gas feeding to the reactor. Four K–type thermocouples are located within the system for temperature measurement: i) one at the exit of the gas preheater; ii) one within the windbox, 0.02 m below the distribution grid; iii) two inside the FB, 0.05 m over the distribution grid and 0.05 m from the reactor wall (middle thermocouple), and 0.08 m above the distribution grid and 0.01 m from the reactor wall (up thermocouple).

The electrically heated FB reactor is depicted in Fig. 3. It features an internal diameter of 0.04 m and, starting from the bottom, is made of two components: i) a windbox section, 0.6 m high, with an upper stainless steel wire mesh serving as gas distributor; ii) a reaction plus freeboard section, 0.8 m high (the relative extension of the two zones depends on the bed inventory). Exhaust gas leaves the reactor at the top of the freeboard. Two semicylindrical radiant heaters (driven by a PID controller) surround the reaction/freeboard zone and the windbox zone for an overall length of about 0.6 m. A lateral port, located a few millimeters above the distribution grid, is used for the simultaneous temperature and pressure measurement inside the FB reactor by a K–type thermocouple and a piezoelectric pressure transducer, respectively. Electronic mass flow controllers are used for gas feeding. The reactor is also equipped with a vacuum system to discharge and collect the bed

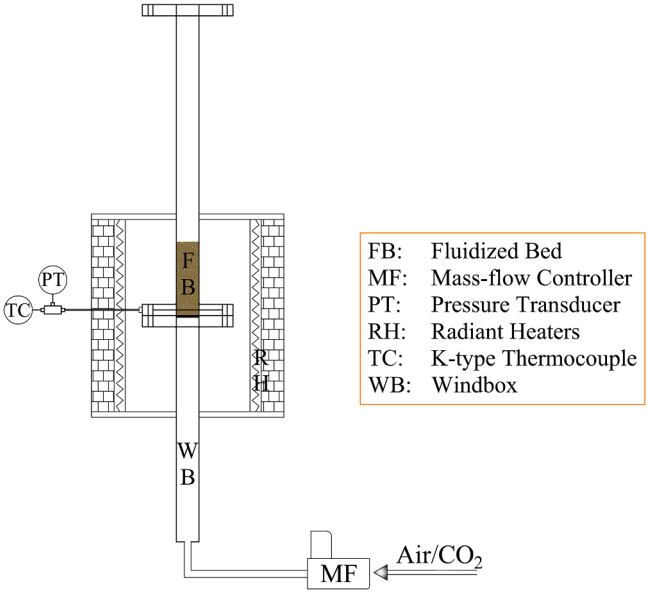

Fig. 3. Electrically heated fluidized bed reactor.

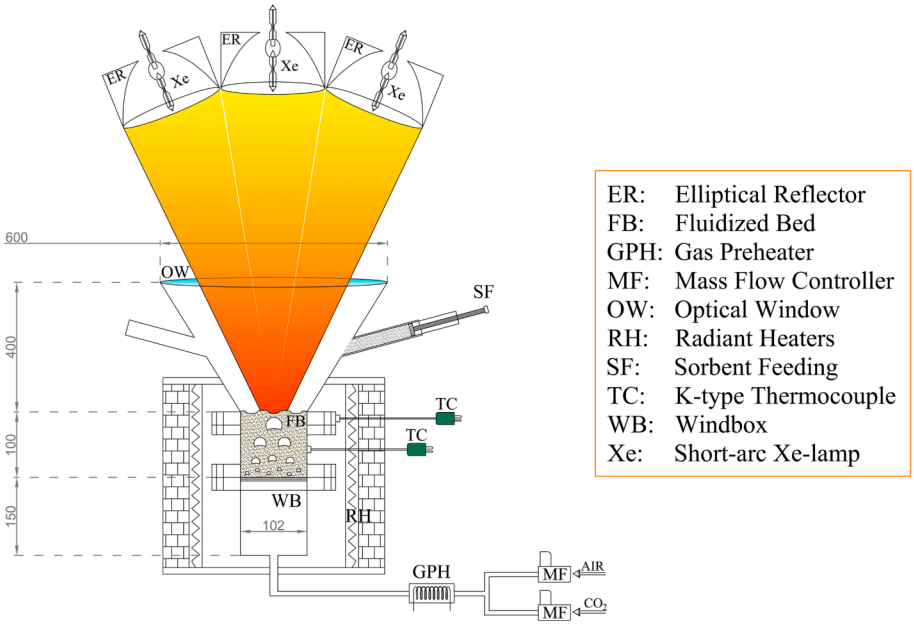

Fig. 2. Directly irradiated fluidized bed reactor. Dimensions in mm.

inventory under cold or hot conditions.

3.2. Materials

Two different materials were used in the experimental campaign: a silica sand from the Ticino river (Italy) and a natural Italian limestone, whose main properties summarized in Table 1. Besides SiO_2 (83.9 $\%_{wt}$), the other constituents of the Ticino sand are Na_2O (1.8 $\%_{wt}$), K_2O (2.4 $\%_{wt}$), CaO (0.9 $\%_{wt}$), MgO (1.0 $\%_{wt}$), Al_2O_3 (8.4 $\%_{wt}$), Fe_2O_3 (1.4 $\%_{wt}$).

3.3. Experimental conditions and procedure

Regardless of the experimental rig, for all the CaL tests performed in this work the following process parameters, relevant to closed loop CaL–CSP integration, were used:

i) reacting atmosphere of 100 $\%_v$ CO_2 during both carbonation and calcination;
ii) reaction time of 20 min for both reaction steps;
iii) superficial gas velocity of 0.6 m s^{-1} throughout the process;
iv) process temperature of 850 °C and 950 °C during carbonation and calcination, respectively.

Moreover, for the experimental runs performed in the directly irradiated FB, bed inventory consisted in a mixture of silica sand (82 $\%_{wt}$) and limestone (18 $\%_{wt}$). Silica sand acts as a thermal flywheel, smoothing and mitigating the temperature variations induced by the chemical reactions. This lime-to-sand ratio was used also in previous experimental campaigns [41,52], and is retained in this work also for a better data comparison. Differently, for the experimental runs performed in the electrically heated FB, bed inventory consisted in either a 1:1 mixture of silica sand and limestone, or limestone only. The smaller scale of the plant allows indeed a better temperature control, offering the possibility of working with higher percentage of lime. This also permitted to perform different characterizations on the reactive material.

3.3.1. Directly irradiated fluidized bed (Experimental procedure #1)

First, the system was charged with ~ 700 g of sand and heated up to 900 °C by the radiant and gas heaters, using air as fluidizing gas. Once achieved this temperature, the fluidizing gas was switched to CO_2 for 5 min to flush all the air from the reactor. The radiant heaters were powered off, and a sample of 150 g of limestone was fed to the reactor. Then, the solar simulator was turned on at the power required to keep the bed at 950 °C to perform the calcination step, assuming as reference the "up" thermocouple. After 20 min (calcination reaction time), the solar simulator was turned off, the fluidizing gas switched to air, and the radiant heaters turned on with a set point temperature of 850 °C. The fluidizing gas was then switched back to CO_2, to perform the carbonation step. After 20 min (carbonation reaction time), the radiant heaters were turned off and the bed was heated up to 950 °C by means of the solar simulator, to perform a new calcination step. The procedure was repeated until completion of 20 looping cycles. At the end of each carbonation step, a small sample of bed material (1–2 g) was collected for the subsequent determination of the carbonation degree of the sorbent. Sand and reactive material were separated by sieving.

Overall, the temperature control in the directly irradiated fluidized bed was quite satisfactory. During the calcination, after the initial transient heating to 950 °C, the average temperature recorded by the up and middle thermocouple was 955 ± 4 °C and 968 ± 5 °C, suggesting a slight bed overheating. During the carbonation, the temperatures recorded by the up and middle thermocouples were in good agreement, with an average value of 838 ± 11 °C.

3.3.2. Electrically heated fluidized bed

Three different experimental procedures were carried out in this facility: a) to assess the sorption degradation of limestone under CaL TCES conditions; b) to assess the interaction of sand presence in limestone degradation under CaL TCES conditions; c) to estimate the minimum fluidization velocity of the calcined and carbonated material upon iterated cycles.

3.3.2.1. Experimental procedure #2. The following experimental procedure was applied to the tests performed with a bed inventory of limestone only. First, the system was charged with ~ 180 g of sand and heated up to 900 °C using air as fluidizing gas. Once achieved this temperature, the vacuum system was used to discharge the bed inventory, and the reactor was cleaned to remove any trace of sand. The fluidizing gas was switched to CO_2, and flowed for 2 min to completely flush the air from the reactor. Then, a sample of 180 g of limestone was fed to the reactor and the PID controller was set to 950 °C to perform the calcination step. After 20 min, heating of the FB was stopped, and the bed inventory was collected by the vacuum system. Before this operation, the fluidizing gas was switched back to air, to prevent a possible sorbent re-carbonation induced by the temperature reduction. The collected material was cooled down to ambient temperature, and weighted. It was then estimated the bulk density of the sample, by pouring the material in a 50 mL graduated cylinder and measuring the weight and occupied volume. Finally, the sample was sieved in the following size ranges: 0–100 μm, 100–200 μm, 300–420 μm and 420–590 μm, and each granulometric cut was individually weighted. All the material was eventually mixed back and fed into the still hot FB reactor under air atmosphere. The PID controller was set to 850 °C and, once reached this temperature, the fluidizing gas was switched to CO_2 to perform the carbonation step. After 20 min, heating of the FB was stopped, and the bed inventory was collected by the vacuum system under CO_2 atmosphere and cooled to ambient temperature. Overall weight (required to evaluate the carbonation degree), bulk density and granulometric distribution were determined as previously described. After that, the sample was fed back to the FB reactor under CO_2 atmosphere, and the PID controller was set to 950 °C, to perform a new calcination step. The procedure was repeated until completion of 20 looping cycles. Overall, the temperature control in the electrically heated fluidized bed was quite effective. During the calcination, apart from a brief overshoot of 10 °C during the initial transient heating to 950 °C, the average temperature was 950 ± 2 °C. Similar fluctuations were observed during the carbonation, with an average temperature of 850 ± 2 °C.

3.3.2.2. Experimental procedure #3. A different experimental run was also performed by applying the same experimental procedure but using a bed inventory of sand and limestone (1:1 weight mixture). Material

Table 1
Main properties of the materials used in the experimental campaign.

Material	Bulk density, tapped [kg m^{-3}]	Size range [μm]	CaO content (calcined material) [$\%_{wt}$]	u'_{mf} (850–950 °C)* [m s^{-1}]
Limestone	1590	420–590	97.4	0.12–0.11
Ticino sand	1489	850–1000	0.9	0.35–0.33

* Minimum fluidization velocity, calculated according to Grace [72].

characterizations were carried out after separation of the sorbent from the sand, performed by sieving. The first calcination was however performed with limestone only, to produce a relevant amount of material for the subsequent cycles.

3.3.2.3. Experimental procedure #4. Finally, to estimate the minimum fluidization velocity, a different experimental run was performed, using again a bed inventory of reactive material only. The same experimental procedure described above was applied but, after each reaction step, the bed inventory was not discharged. Instead, an automated script developed in LABVIEW was run to measure the pressure drop vs. the superficial gas velocity in a "down–curve" from 30 to 0 cm s^{-1}, with 1 cm s^{-1} step. Curves were acquired at the process temperature of the relevant step, using CO_2 as fluidizing gas. Particular accuracy was dedicated to ensuring the temperature uniformity of the entire fluidized bed when decreasing the superficial gas velocity. To this aim, the bed was vigorously fluidized before the acquisition of each pressure drop measurement.

3.4. Data analysis and further characterization

The mean carbonation degree for the tests performed in the directly irradiated FB was evaluated using the samples of carbonated material collected after each carbonation step. The samples were individually calcined in a muffle furnace at 950 °C under air atmosphere, and the weight change was measured with an analytical balance (0.1 mg precision), so as to determine the mean carbonation degree as described in Di Lauro et al. [52].

For the tests performed in the electrically heated FB, the data of overall weight after each reaction step were used to compute the mean carbonation degree ($\overline{X}_{Ca}$) as:

$$\overline{X}_{Ca}(N) = \frac{\left(m_N^{carb} - m_{N-1}^{calc}\right)}{m_{N-1}^{calc} x_{CaO}} \frac{MW_{CaO}}{MW_{CO_2}} \quad (1)$$

where N is an index for the cycle number, m^{carb} and m^{calc} represent the overall weight of the carbonated and calcined sample, respectively, x_{CaO} is the mass fraction of CaO in the calcined sorbent (see Table 1), MW stands for molecular weight.

Mean carbonation degree data were further processed to compute the average energy storage density (E_{SD}) following the methodology described in Di Lauro et al. [52]. Computed values account for both the chemical heat and sensible heat contributions.

Data of Particle Size Distribution (PSD) were post–processed to evaluate the mean Sauter diameter.

The curves of pressure drop vs. superficial gas velocity were analyzed to compute the minimum fluidization velocity of the calcined and carbonated particles.

Finally, samples of lime retrieved after the last calcination step were subjected to X-Ray Diffraction (XRD) analysis, performed using a Rigaku MiniFlex 600 instrument, and to N_2–intrusion porosimetric analyses to investigate differences in specific surface area (through BET theory), total pore volume and pore size distribution (through BJH theory).

4. Results

4.1. Sorbent carbonation degree

Fig. 4 shows the mean carbonation degree of the sorbent obtained in the different experimental tests (*EP #1*, *#2* and *#3*). It is possible to observe that the mean carbonation degree decreases along with reaction cycles. Sintering phenomena and loss of reactivity are induced by the high temperature and high CO_2 concentration experienced by the sorbent during both reaction steps. With reference to experimental tests performed in the directly irradiated FB (*EP#1* where solid inventory includes limestone and sand), $\overline{X}_{Ca}$ decreases from about 61% ($N = 1$) to about 4% ($N = 20$), with an average value of 14% over the whole 20 reaction cycles. Performance of the tests carried out in the electrically heated FB with a bed inventory of limestone and sand (*EP #3*) do not differ sensibly: $\overline{X}_{Ca}$ decreases from about 60% ($N = 1$) to about 8% ($N = 20$), with an average value of 16% over the whole reaction cycles. The slightly worse performance achieved in the directly irradiated FB may be caused by the overheating of the bed surface induced by the highly concentrated solar radiation, as observed in previous research studies [11]. The temperature difference between the "middle" and "up" thermocouple ranged within 13.4 ± 3.2 °C across the different tests. The bed surface overheating was not measured in this work, but according to previous experimental studies it can be as high as 80 °C in the centre of the FB [11,41]. Differently, the tests performed in the electrically heated FB with a bed inventory of limestone only (*EP #2*) show better performance in terms of sorbent reactivity. The mean carbonation degree decreases indeed from about 62% (1st cycle) to about 14% (20th cycle), with an average value over the whole 20 cycles of about 25%. This was an unexpected result that needed further investigation. In particular, it was scrutinized in literature a possible chemical interaction between the silica sand constituents and lime particles, with the formation of unreactive compounds, which can subtract reactive CaO, and induce a loss of reactivity. Dicalcium silicate (Ca_2SiO_4, i.e. belite), one of the main constituents of the Portland cement clinker [73,74], is formed when raw meals for cement production are used as sorbents in CaL process for CO_2 capture [75]. It was claimed that its formation reduces the CO_2 sorption capacity of the cement raw meals subtracting CaO sites available for the carbonation reaction [76]. Valverde et al. [77] also observed the formation of calcium silicates from the interaction of a calcium-based sorbent and a SiO_2 nanostructured powder under CaL conditions. However, in this case the addition of nanostructured SiO_2 increases the carbonation degree improving the CO_2 accessibility to the CaO sites. Experimental data plotted in Fig. 4 shows a detrimental effect of Ticino silica sand on lime reactivity, in analogy with the findings obtained with cement raw meals used in CaL process for CO_2 capture [75]. A further consequence of this result is related to the use of additives, devoted to improving the fluidizability of small particles of limestone and/or its optical performance in terms of absorption of concentrated solar energy. Their addition to sorbent particles should be carefully evaluated because of possible interaction with lime and consequent decrease in reactivity.

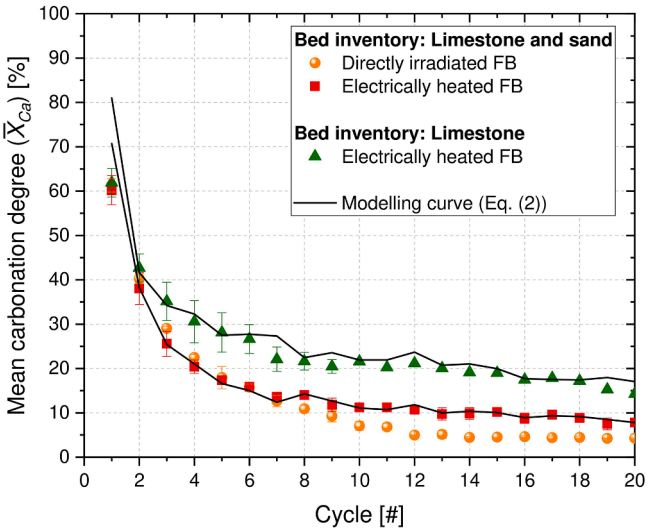

Fig. 4. Mean carbonation degree of the sorbent as a function of the cycle number and of the adopted operating conditions.

Post-processing of $\overline{X}_{Ca}(N)$ data has been carried out by postulating here the following IAD "Initial Activity Decay" equation:

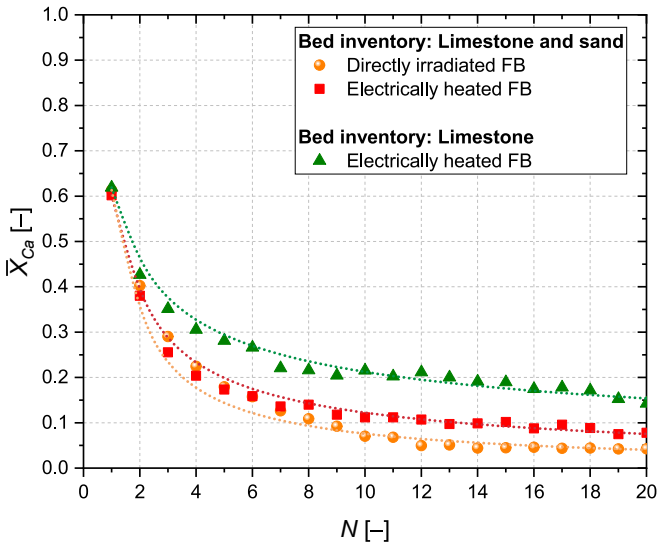

Fig. 5. Fitting of experimental carbonation degree data by the IAD Eq. (2).

Table 2
Values for the decay constant (IAD model) for the cases under investigation.

	k_2 [–]	R^2 [–]
Limestone and sand inventory Directly irradiated FB	0.91	0.97
Limestone and sand inventory Electrically heated FB	0.69	0.98
Limestone inventory Electrically heated FB	0.46	0.97

$$\overline{X}_{Ca}(N) = k_1 N^{-k_2} \quad (2)$$

where k_1 is the initial activity constant, that measures the efficacy of the sorbent when $N = 1$ ($\overline{X}_{Ca}(N = 1) = k_1$), and k_2 is the decay constant that considers the resistance of the sorbent to sintering phenomena (the higher k_2, the worst the sintering resistance). While Fig. 5 shows data fitting, Table 2 lists the best-fitting values for k_2 (along with the values for the coefficient of determination). Sintering resistance for the sorbent

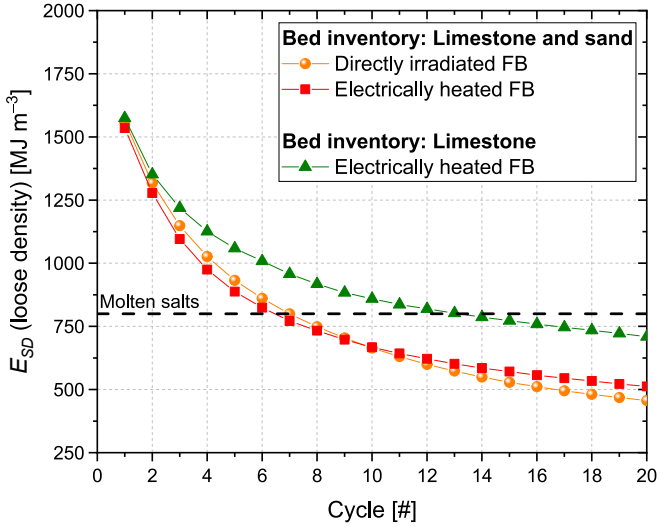

Fig. 6. Average energy storage density up to the reaction cycle considered vs. reaction stage, under the adopted operating conditions.

in the case of limestone inventory and electrically heated FB (*EP #2*) resulted ca. 33% and 49% higher vs. the cases with limestone and sand inventory (electrically heated (*EP #3*) and directly irradiated FB (*EP #1*), respectively), to confirm the ranking discussed above.

4.2. Density of energy storage

Fig. 6 shows the average values of energy storage density up to the reaction cycle considered vs. reaction cycle, for the different experimental runs. Data were computed under a conservative scenario by considering the loose density of limestone, which is about 13% lower than the tapped density value [52]. The energy storage density of the molten salts is also plotted as reference material, though a more comprehensive comparison should also account for the different technology and operating conditions of the two processes (i.e., thermal energy storage with molten salts and TCES with CaL). For the tests with a bed inventory of limestone and sand, the average values of E_{SD} are quite similar for the two experimental rigs and decrease from about 1550 MJ m^{-3} (1 looping cycle) to 485 MJ m^{-3} (20 looping cycles). Under these process conditions, the CaL system outperforms the molten salts one only up to an average sorbent life of 6 cycles. From the 8th cycle onwards, the molten salts system appears to be superior. Data obtained in this study appear to be worse than those shown in Di Lauro et al. [52] for limestone in closed loop configuration, where carbonation was performed at 650 °C and 15 %$_v$ CO_2. This arises because of: i) a slightly lower reactivity of the sorbent in the present study, probably induced by the higher temperature and CO_2 concentration experienced during carbonation (mean carbonation degree at the 20th reaction cycle is of 13.7% in this work vs. 15.3% in Di Lauro et al. [52]); ii) a lower amount of sensible energy storage in this work (to perform carbonation, CaO is cooled from 950 °C to 850 °C in this work and from 950 °C to 650 °C in Di Lauro et al. [52]). Data of E_{SD} obtained with a bed inventory of limestone only are slightly better, especially at increasing looping cycles. Values decrease from about 1575 MJ m^{-3} (1 looping cycle) to 710 MJ m^{-3} (20 looping cycles). Even if the performance in terms of E_{SD} is comparable to that of molten salts when an average sorbent life of 10–20 cycles is considered, it should be recalled that, in this CaL process, thermal energy at the carbonator is released at a much higher temperature (i.e., 850 °C), with a consequent higher overall efficiency in the subsequent thermodynamic cycle for energy production. Moreover, the share of chemical heat storage over the total is very high. It values about 91% at the first cycle for all the tests, and decreases to 79% (10 looping cycles) and 70% (20 looping cycles) for the tests performed with a bed inventory of lime and sand, and to 84% (10 looping cycles) and 80% (20 looping cycles) for the tests performed with a bed inventory of limestone only.

4.3. Particle size distribution

Fig. 7 shows information on the attrition/fragmentation of the bed inventory for the experimental runs performed in the electrically heated FB. Data are plotted either as cumulative PSD for selected calcination stages (Fig. 7–A) or as mean Sauter diameter (d_{Sauter}) vs. reaction number (Fig. 7–B).

Figure 7–A highlights a progressive fragmentation/shrinkage of limestone particles along with reaction cycles. Particles mostly shift from the 420–590 μm to the 300–400 μm size range, whereas the mass fraction of smaller size ranges (less than 300 μm) only slightly increases. The effect is more pronounced for the tests performed with a bed inventory of limestone and sand, suggesting that the presence of sand enhances the fragmentation/shrinkage of limestone particles. Particle size reduction appears to be mostly concluded at the 10th calcination for tests with a bed inventory of limestone only, as the PSD for the 10th and 20th calcined samples mostly overlap. Differently, when the bed inventory of limestone and sand is used, the PSD for the 10th and 20th calcined samples still shows significant differences. Discussed data are

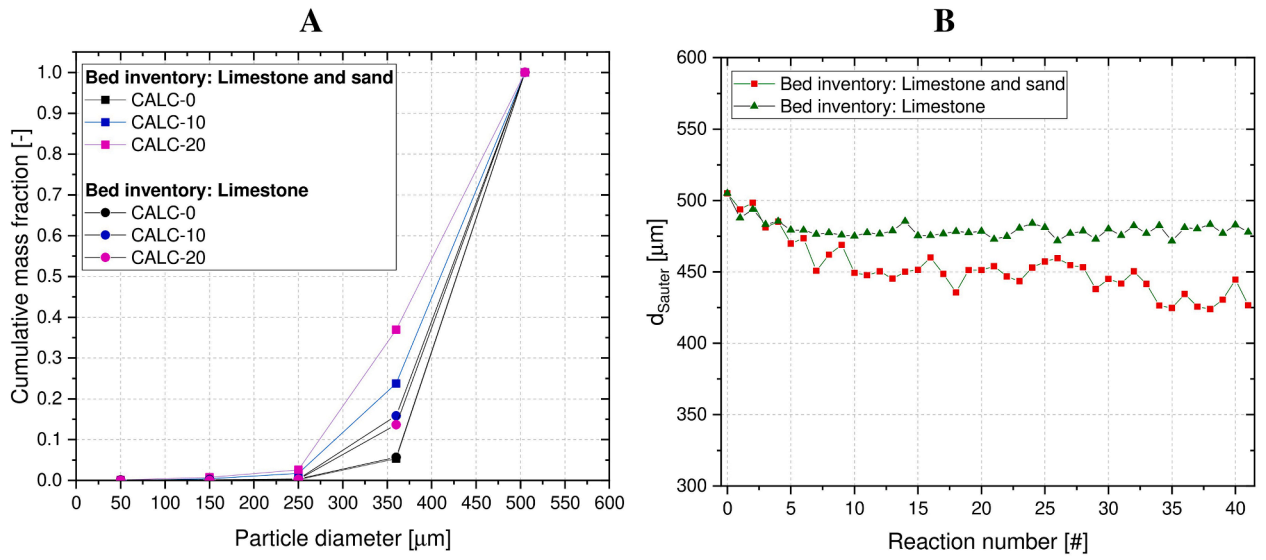

Fig. 7. A) Cumulative particle size distribution for selected calcination stages (CALC-0 refers to the samples after the initial calcination); B) Mean Sauter diameter of the bed inventory vs. reaction number (reaction number 0 refers to the starting limestone samples).

further confirmed by the trend of d_{Sauter} highlighted in Fig. 7–B. Starting from the 505 μm value of the limestone samples fed to the reactor, d_{Sauter} decreases to about 475 μm and 425 μm for the tests with a bed inventory of limestone only and limestone and sand, respectively. With regards to tests with limestone only, the value of 475 μm is approached already at the 10th reaction step (corresponding to the 5th carbonation). Differently, tests with a bed inventory of limestone and sand show a first stabilization of d_{Sauter} at about 450 μm from the 10th reaction step on, followed by a second decrease towards 425 μm from the 30th reaction step on, which suggests a further weakening/shrinkage of the material structure upon iterated reaction cycles. Fig. 7 also highlights that, in both tests, the fraction of material below 150 μm is mostly negligible, as it always accounts for less than 1%. It is reasonable that finer particles are also formed during the process, but are elutriated from the system. For this reason, the make-up stream of fresh limestone used in the process (see Fig. 1), should be intended to also compensate for this net mass loss [67].

4.4. Particle density

Fig. 8 shows the bulk density of limestone particles after each reaction step for the tests performed with the bed inventory of limestone and sand and limestone only. As expected, the density values of calcined particles are always lower than those of the corresponding carbonated ones. However, the trend of density with reaction stage quite differs for the two experimental tests. Indeed, in tests with sand, the density of the calcined particles increases along with reaction cycles, whereas that of the carbonated particles is mostly constant after a decrease during the very first cycles. Differently, in tests without sand, the density of the calcined particles is mostly constant after an increase during the first reaction cycles, whereas that of the carbonated particles decreases along with the reaction cycles, especially during the first 8 carbonation steps. Further, for both carbonated and calcined particles, the density values obtained in tests with sand are always higher than those obtained in tests without sand. Data obtained when working with the bed inventory of limestone only are probably the easiest to explain: the density of carbonated samples decreases with reaction cycles because of the lower carbonation degree as the number of cycles progresses, whereas the density of calcined samples is mostly constant after a first increase resulting upon loss of porosity. Differently, data obtained when working with sand show that the density of the calcined samples increases because of the interaction with sand, whereas that of the carbonated samples remains mostly constant because the decrease induced by the lower carbonation degree is offset by the increase induced by the interaction with sand. This explanation is further corroborated by the higher density values detected in tests with sand. Data were post-processed to evaluate the density increase that could have been induced from belite formation, quantitatively evaluated on the basis of the reduction of carbonation degree [75,76] with respect to the tests without sand. It was found that the formation of belite can only justify an increase of 5% of materials density. It is noteworthy that the sand may also physically act on the sorbent particles reducing their porosity and, in turn, increasing the particle density of both calcined and carbonated samples.

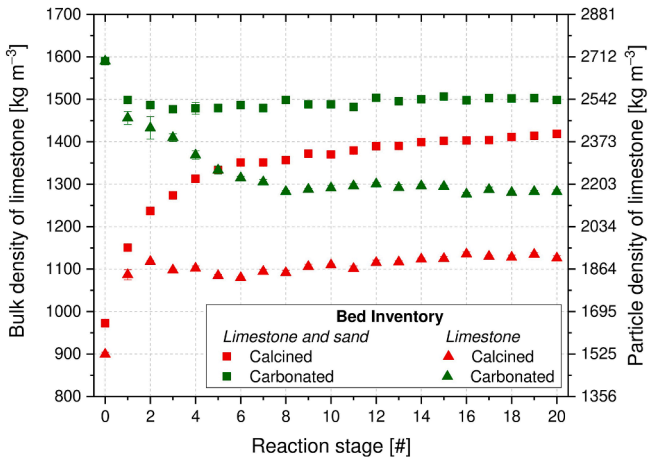

Fig. 8. Bulk and particle density of limestone particles for calcined and carbonated samples, in tests performed with a bed inventory of limestone and sand, and limestone only.

The bulk density of the calcined and carbonated samples upon iterated cycles has been further worked out to better correlate the physical properties of the granular solids along the course of the CaL process. In particular, the obtained data can be used to estimate the mean conversion degree during the carbonation step, and the particle density and porosity of the calcined and carbonated samples, upon calcination/carbonation iterated cycles.

The mean carbonation degree can be calculated exclusively by the bulk density of batches of calcined and carbonated particles once it is

assumed that the volume occupied by the granular solids does not significantly change during each single carbonation step. Equation (1) can then be rearranged as:

$$\overline{X}_{Ca}(N) = \left(\frac{\rho_N^{carb} V_N^{carb} - \rho_{N-1}^{calc} V_{N-1}^{calc}}{\rho_{N-1}^{calc} V_{N-1}^{calc}}\right) \frac{MW_{CaO}}{x_{CaO} MW_{CO_2}} \approx \left(\frac{\rho_N^{carb}}{\rho_{N-1}^{calc}} - 1\right) \frac{MW_{CaO}}{x_{CaO} MW_{CO_2}} \tag{3}$$

where ρ^{carb} and ρ^{calc} are the bulk density of the carbonated and calcined particles, respectively, and V^{carb} and V^{calc} represent the volume occupied by the bed of carbonated and calcined particles, respectively. The results obtained from Eq. (3) are reported in Fig. 4 and, thereby, compared with the conversion degree calculated by Eq. (1). The comparison highlights that the method based on the measurements of bulk densities accurately agrees with the data obtained from samples weight. This result can be used to set up alternative methods to estimate the conversion degree during the carbonation step in, even large-scale, CaL systems, simply sampling the granular solids both first and after each carbonation step.

The particle density of the calcined and carbonated materials at a generic N cycle, ρ_{pN}^{calc} and ρ_{pN}^{carb}, respectively, can be estimated from the corresponding bulk densities by the following equations:

$$\rho_{pN}^{calc} = \frac{\rho_N^{calc}}{1 - \varepsilon_{bedN}^{calc}}; \quad \rho_{pN}^{carb} = \frac{\rho_N^{carb}}{1 - \varepsilon_{bedN}^{carb}} \tag{4}$$

where $\varepsilon_{bedN}^{calc}$ and $\varepsilon_{bedN}^{carb}$ are the bed voidage during the bulk density measurement for the calcined and carbonated materials at a generic N cycle, respectively. Assuming a constant bed voidage equal to 0.41, a typical value for packed bed, the particle density can be easily evaluated, and the obtained data points can be read in Fig. 8 together with the bulk density values.

The particle porosity of the calcined and carbonated particles, in turn, can be calculated by the following equations, assuming as reference the density of pure CaO for the calcined particles, and a mean value (based on the carbonation degree) between the density of pure CaO and $CaCO_3$, for the carbonated particles:

$$\varepsilon_{pN}^{calc} = 1 - \frac{\rho_N^{calc}}{\rho_{CaO}};$$

$$\varepsilon_{pN}^{carb} = 1 - \frac{\rho_N^{carb}}{\frac{\overline{X}_{Ca}(N) MW_{CaCO_3} + (1 - \overline{X}_{Ca}(N)) MW_{CaO}}{\frac{\overline{X}_{Ca}(N) MW_{CaCO_3}}{\rho_{CaCO_3}} + \frac{(1 - \overline{X}_{Ca}(N)) MW_{CaO}}{\rho_{CaO}}}} \tag{5}$$

where ρ_{CaO} and ρ_{CaCO_3} are the density of pure CaO and $CaCO_3$, set equal to 3340 kg m^{-3} and 2710 kg m^{-3}, respectively. It is worth to note that the contribution of solid compounds, formed by the chemical interaction between lime and silica sand, to the absolute particle density has been neglected.

Finally, it can be defined as "reactive" the porosity that vanishes during the carbonation step as:

$$\varepsilon_{pN}^{react} = \varepsilon_{pN-1}^{calc} - \varepsilon_{pN}^{carb} \tag{6}$$

The "reactive" porosity represents the internal porosity of the particles, which is occupied by the CO_2 molecules reacting with CaO to form $CaCO_3$ during the carbonation step. The particle porosity and the "reactive" porosity are shown as a function of the reaction stage in Fig. 9 for all the investigated conditions.

Data in Fig. 9-A counter-mirror those of Fig. 8. The analysis of the data of particle porosity for the samples obtained processing only limestone particles highlights, as also reported in literature [78], that the reduction of reactivity of limestone is due to the reduction of porosity of the calcined particles during the first cycles, and the concurrent sintering of the carbonated particles along the iterated cycles. The porosity of carbonated particles increases upon iterated cycles in agreement with a larger amount of porosity no more accessible by CO_2 molecules during carbonation. A different scenario appears when analyzing the experimental data of the tests carried out using limestone with silica sand particles. The interaction with silica sand particles strongly influences the phenomenology: the porosity of calcined particles steadily decreases along the iterated cycles, whereas the porosity of carbonated particles increases only during the first cycles. Moreover, in presence of sand, particle porosity values are remarkably lower than the corresponding ones in the case without sand. The "reactive" porosity trend along iterated cycles (Fig. 9-B) confirms what already observed, and highlights a difference in the "reactive" porosity of about 0.04 in favour of the only limestone case.

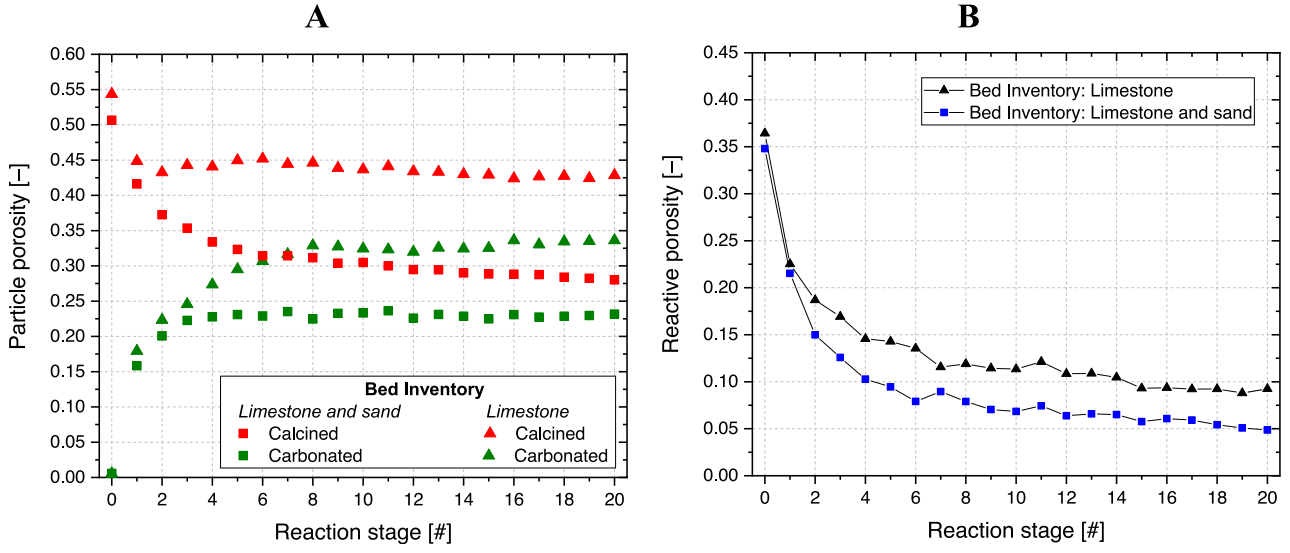

Fig. 9. Particle (A) and "reactive" (B) porosity of limestone particles for calcined and carbonated samples in tests performed with a bed inventory of limestone and sand, and limestone only.

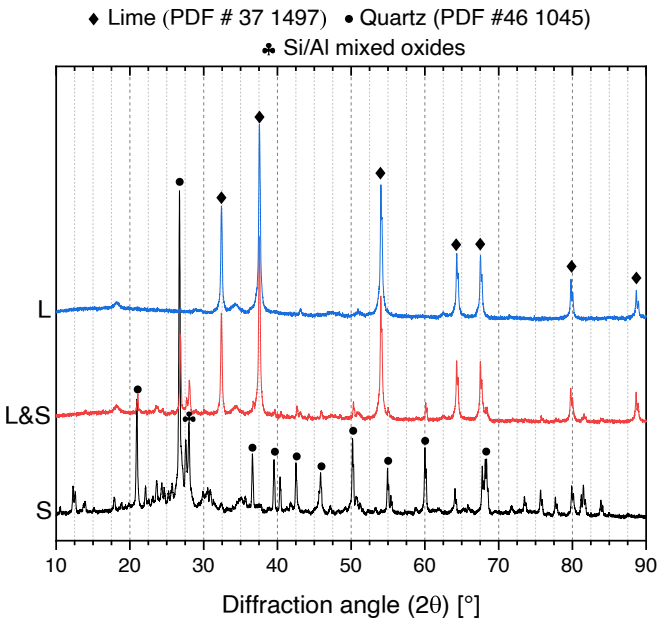

Fig. 10. XRD profiles of: lime samples retrieved after the last calcination step in the electrically heated FB, for tests performed with a bed inventory of limestone only (L) and limestone and sand (L&S); pure sand (S).

4.5. XRD and visual analyses

Fig. 10 shows the XRD profiles of the lime samples retrieved after the last calcination step for the tests performed in the electrically heated FB, together with that of pure sand. It is possible to observe that:

- the XRD spectrum of the sand exhibits several characteristics peaks of quartz (SiO_2), and a few minor peaks related to other compounds and impurities present in the sample;
- the XRD spectrum of the calcined sample retrieved from the tests performed with a bed inventory of limestone only exactly matches the crystalline signature of lime (CaO);
- the XRD spectrum of the calcined sample retrieved from the tests performed with a bed inventory of limestone and sand exhibits, apart from the peaks related to lime, several additional peaks that match either those of quartz, or those of the other compounds found in the sand.

XRD data seems to rule out a bulk chemical interaction between sand and lime since no peaks related to new crystalline phases were detected. It is likely that a potential chemical interaction takes place only at the particle surface, given the sizes of sorbent and sand particles used in this study. For the sake of completeness, it should be underlined that sand-derived peaks found in the calcined sample may arise, apart from very fine sand particles trapped in the lime pores, also from sand particles that, upon iterated attrition/fragmentation, approached the size of lime ones and were thus not trapped by the sieves. A quantitative XRD analysis was also performed to assess the extent of sand contamination, and of belite formation. Belite formation was again not detected while the sand percentage turned out to be 5–6%. Such low values cannot justify the density differences observed in the two samples, and support the discussion on the reduction of particles porosity previously highlighted (see §4.4).

Fig. 11 shows a picture of these three samples. The comparison highlights that lime particles retrieved from the test performed with a bed inventory of sand and lime features a slightly darker colour, probably as a consequence of the physical and chemical interaction with the sand.

4.6. Porosimetric analyses

The results of the porosimetric analyses reveal that the specific surface is quite low in all the samples (1–2 $m^2\ g^{-1}$) calcined at the 20th cycle, and similar to values reported in other studies under severe calcination conditions [41]. The cumulative pore volume distribution of the different samples is, instead, shown in Fig. 12. The lime sample processed in the electrically heated FB without sand, that is the best in terms of mean carbonation degree, is characterized by the highest value of total pore volume (0.165 $cm^3\ g^{-1}$), mostly of which are mesopores (~88%). When lime is processed together with sand, the distribution is quite different depending on the reactor used. Lime processed in the electrically heated FB, that has intermediate performance in terms of mean carbonation degree, has the lowest value of total pore volume (0.047 $cm^3\ g^{-1}$) but a significant share of both micropores and smaller mesopores (~80%), probably formed due to the sand/sorbent interaction. Differently, lime processed in the directly irradiated FB, that has the worst performance in terms of mean carbonation degree, has an intermediate value of total pore volume (0.106 $cm^3\ g^{-1}$), but half of them are macropores and are thus less relevant for the reactivity of the material. The formation of larger pores may have been induced by the thermal sintering due the bed surface overheating produced by the simulated solar radiation. It seems that the sand/sorbent interaction might have played a less important role in these tests, probably due to the different hydrodynamics related to the larger scale of the used reactor.

4.7. Minimum fluidization velocity

Fig. 13 shows the minimum fluidization velocity of carbonated and calcined samples in tests performed using a bed inventory of limestone only (*EP #4*). It is recalled that data were acquired at the process temperature of the reaction step (i.e., 850 °C for carbonation, 950 °C for calcination), using CO_2 as fluidizing gas. The trend of the minimum fluidization velocity recalls that of the bulk density (see Fig. 8). For calcined samples, the minimum fluidization velocity slightly increases

Fig. 11. Picture of: lime samples retrieved after the last calcination step in the electrically heated FB, for tests performed with a bed inventory of limestone only (L) and limestone and sand (L&S); pure sand (S).

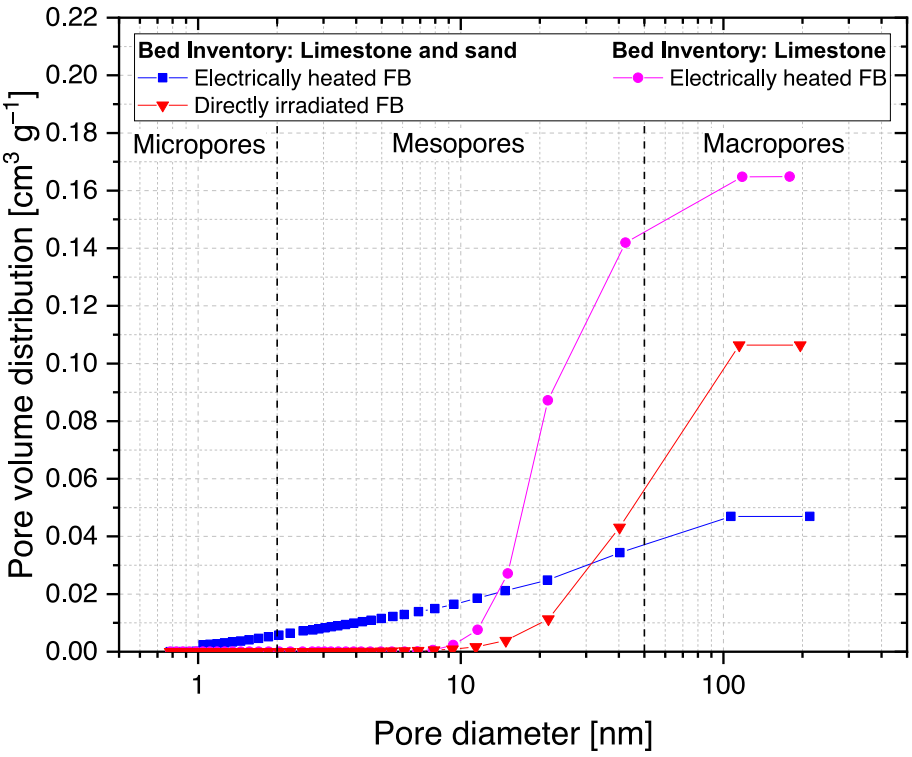

Fig. 12. Cumulative pore volume distribution of the different samples, after the last calcination step.

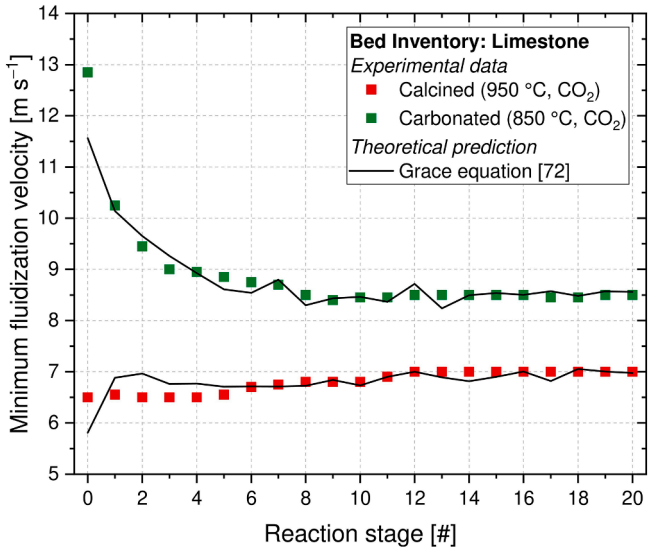

Fig. 13. Minimum fluidization velocity for calcined and carbonated sorbent samples at the relevant process temperature, using CO_2 as fluidizing gas, obtained from experimental data and theoretical approach.

from an initial value of about 6.5 cm s^{-1} (initial calcination) to about 7 cm s^{-1} (20^{th} reaction stage). Conversely, for carbonated samples, the minimum fluidization velocity decreases from about 10.2 cm s^{-1} (1^{st} reaction stage) to about 8.5 cm s^{-1} (20^{th} reaction stage). Overall, a difference between the minimum fluidization velocity of carbonated and calcined samples of about 3.7 cm s^{-1} can be inferred for more reactive particles, which decreases to about 1.5 cm s^{-1} for less reactive ones. The obtained experimental data were compared with those calculated by the semi-empirical correlation proposed by Grace (Eq. (7)) [72]:

$$\frac{d_p u_{mf} \rho}{\mu} = \left[27.2^2 + 0.0408 \frac{d_p^3 \rho (\rho_p - \rho) g}{\mu^2}\right]^{1/2} - 27.2 \quad (7)$$

where d_p is the particle diameter, u_{mf} the minimum fluidization velocity, ρ and ρ_p the gas and particle density, respectively, μ the dynamic gas viscosity, and g the gravitational acceleration. Particle size and density data used in Eq. (7) are those reported in Fig. 7–B and 8, respectively. The comparison shows a very satisfactory agreement, confirming the approach proposed with Eq. (4). According to these data, it could be speculated that a solid–solid fluidized bed separation may be feasible at least to some extent, to separate the more reacted particles from the less reacted ones. The exploitation of a fluidized bed classifier, already proposed in literature [70], could be explored for an efficient separation of the investigated granular solids.

5. Discussion

On the whole, the analysis of the experimental results discussed in the present work returns two key findings.

Co-processing of limestone with silica sand reduces the lime reactivity, as inferred from the lower values of mean carbonation degree. Post-process of density data, together with N_2-intrusion porosimetric analysis, and quantitative and qualitative XRD analyses, suggests that this effect is mainly due to a lime/sand mechanical interaction that induces a strong reduction of the total and reactive sorbent porosity. A chemical interaction between CaO and silica sand constituents, not detected by XRD analyses, might only occur at particle surface and to a small extent, and could not justify alone the decay of reactivity observed when coprocessing lime with silica sand. The detrimental effect of this interaction on the CaL performance poses concerns to the use of additives to improve the fluidizability of small particles of limestone and/or to improve its optical performance in terms of absorption of concentrated solar energy. Under the tested conditions, the density of energy storage of limestone co-processed with silica sand becomes lower than that of the molten salts after 7 reaction cycles. However, the stored

energy can be released at higher temperatures, allowing for higher process efficiency in the thermodynamic cycle for energy generation, and is retained in a more stable form, suitable also for seasonal energy storage. Using a bed of only limestone may produce better results, as the density of energy storage is only slightly lower than that of molten salts after 20 cycles. However, this solution might require more efforts in the design of the receiver to reduce the share of reflected or unabsorbed solar energy, by considering for instance "creative" and non-conventional solar particle receivers [8,79,80]. According to these findings, it is advised to consider materials different from sand, if additives need to be used. A good inert material should perform a twofold task. On one side, it should increase the absorption of solar energy, as natural limestone particles have a poor solar optical absorption. On the other side, it should not chemically/physically interact with limestone particles, and possibly shield them from the high concentrated solar radiation. In this way, the performance of the process might reach the higher values obtained in this study with pure limestone and electrical heating. Alternatively, synthetic CaO-based sorbents should be considered. Thanks to the addition of inert stabilizers and/or promoters, these materials are characterized by a lower decay of reactivity over cycling and feature thus higher energy storage densities [27,42]. It is noteworthy that the doping of CaO-based sorbents has been recently targeted to also increase the absorption of solar energy [42,58,59], thus simultaneously counteracting two relevant drawbacks of the CaL cycle for TCES. Finally, it is also recalled that the average life of the sorbent particles in a continuous CaL process is controlled by the fraction of the purge and make-up streams (see Fig. 1). Typically, a purge fraction of 5–10% of the looping streams is considered in literature [67,68] and, in turn, the sorbent particles experience about 20–10 calcination/carbonation cycles, respectively, before they are purged. Thus, in any case, a sudden reactivity decay of sorbent can always be counterbalanced by a further increase of the make-up/purge fraction, which decreases the average life of the sorbent particles and thus increases their energy storage density [41,52]. It is noteworthy that the purge stream of spent sorbent particles does not represent a net energy loss for the process, as it can be reused as raw feedstock in the cement industry [41,73,81,82].

Carbonated and calcined particles are characterized by a different density and porosity, that results into a sufficient difference in their minimum fluidization velocity. This difference may be exploited for the design of a fluidized bed classifier that recycles unreacted or less reacted particles to the carbonator. In this way, it would be possible to maximize the efficiency of the process by ensuring the maximum carbonation degree of sorbent particles, and by avoiding the circulation of streams of unreacted particles through the plant. It is noteworthy that the effective advantage brought by the classifier is strictly related to the material reactivity and resistance to sintering over cycling. When the reactivity of the material abruptly decreases over cycling the efficacy of the classifier is probably lower, as the increase in conversion degree that could be obtained from the material recycling is smaller. However, synthetic sorbents feature a much stronger resistance to sintering, and are able to preserve better their initial reactivity over cycling. In this case, the contribution of the classifier to the overall process efficiency may be much higher.

Further tests will be performed in future works to fully demonstrate the feasibility and efficiency of the FB classifier, and to estimate its contribution to the overall efficiency of the process. Moreover, different inert materials will be tested in mixture with lime, and in different ratio, to scrutinize their potential advantages and drawbacks in the CaL process for TCES.

6. Conclusions

The calcium looping process integrated with TCES has been investigated focusing the attention on the closed loop CO_2 scheme with carbonation/calcination at 850/950 °C under pure CO_2. In particular, the conditions needed for the addition of a solid–solid separation unit after the carbonator to separate converted and unconverted particles and, consequently, to increase the process efficiency, have been analyzed. The experimental tests, performed in the directly irradiated FB, show that the mean carbonation degree decreases from about 61% (1^{st} cycle) to about 4% (20^{th} cycle), with an average value of 14% over the whole 20 reaction cycles. Similar results are obtained in the electrically heated FB with a bed inventory of limestone and sand. Differently, the tests performed in the same reactor with a bed inventory of limestone show superior performance: the mean carbonation degree decreases indeed from about 62% (1^{st} cycle) to about 14% (20^{th} cycle), with an average value over the whole 20 cycles of about 25% (data were confirmed by evaluation of the deactivation constant, obtained by the application of an initial activity decay equation). It seems that the chemical interaction of CaO with the silica sand constituents at the process temperatures is not the main responsible for the loss of reactive CaO toward CO_2 uptake. Instead, post-process of particle density data, together with N_2-intrusion porosimetric analysis, and quantitative and qualitative XRD analyses, suggests that the sand/lime mechanical interaction induces a strong reduction of the total and reactive sorbent porosity that is the main responsible for the strong decay of reactivity. The detrimental effect of this interaction on the calcium looping performance poses concerns to the use of additives to improve the fluidizability of small particles of limestone and/or to improve its optical performance in terms of absorption of concentrated solar energy. For the tests with a bed inventory of limestone and sand, the average values of energy storage density are quite similar for the two experimental rigs and decrease from about 1550 MJ m^{-3} (1 looping cycle) to 485 MJ m^{-3} (20 looping cycles). Instead, with a bed inventory of limestone, the values decrease from about 1575 MJ m^{-3} (1 looping cycle) to 710 MJ m^{-3} (20 looping cycles). The performance in terms of energy storage density is comparable to that of molten salts when an average sorbent life of 10–20 cycles is considered. However, it should be recalled that, in this CaL process, thermal energy at the carbonator is released at a much higher temperature (i.e., 850 °C), with a consequent higher overall efficiency in the subsequent thermodynamic cycle for energy production. The main properties of calcined and carbonated particles significantly change in terms of particle density, size and porosity, if the limestone is processed with silica sand fluidized particles. Finally, the measurements of minimum fluidization velocity of calcined and carbonated particles upon iterated cycles of calcination and carbonation show that a solid–solid separation based on particle density difference may be conceived by a fluidized bed classifier already proposed in literature [70].

Declaration of Competing Interest

The authors declare that they have no known competing financial interests or personal relationships that could have appeared to influence the work reported in this paper.

Data availability

Data will be made available on request.

Acknowledgments

The support of Ms. Laura Garofalo, Mr. Sebastiano Minale, and Mr. Francesco Valerio Vitiello in the experimental campaign is gratefully acknowledged. Mr. Luciano Cortese, Dr. Renata Migliaccio and Dr. Odda Ruiz de Ballesteros are acknowledged for their help in carrying out qualitative and quantitative XRD analyses. The FPU Programme and the mobility grant for FPU beneficiaries of the Spanish Ministry of Science, Innovation and Universities (FPU2017/03902 and EST19/00144) provided financial support for Sara Pascual PhD studies.

References

[1] H. Zhang, H. Benoit, I. Perez-Lopèz, G. Flamant, T. Tan, J. Baeyens, High-efficiency solar power towers using particle suspensions as heat carrier in the receiver and in the thermal energy storage, Renew. Energy. 111 (2017) 438–446, https://doi.org/10.1016/j.renene.2017.03.101.

[2] C. Tregambi, S. Padula, M. Galbusieri, G. Coppola, F. Montagnaro, P. Salatino, M. Troiano, R. Solimene, Directly irradiated fluidized bed reactor for thermochemical energy storage and solar fuels production, Powder Technol. 366 (2020) 460–469, https://doi.org/10.1016/j.powtec.2020.02.045.

[3] C.K. Ho, Advances in central receivers for concentrating solar applications, Sol. Energy. 152 (2017) 38–56, https://doi.org/10.1016/j.solener.2017.03.048.

[4] A. Bayon, A.J. Carrillo, E. Mastronardo, J.M. Coronado, Chapter Six - Thermochemical heat storage at high temperature, in: W. Lipiński (Ed.), Sol. Thermochem., Academic Press, 2021: pp. 247–295. https://doi.org/10.1016/bs.ache.2021.10.004.

[5] A.J. Carrillo, J. González-Aguilar, M. Romero, J.M. Coronado, Solar Energy on Demand: A Review on High Temperature Thermochemical Heat Storage Systems and Materials, Chem. Rev. 119 (2019) 4777–4816, https://doi.org/10.1021/acs.chemrev.8b00315.

[6] W. Lipiński, E. Abbasi-Shavazi, J. Chen, J. Coventry, M. Hangi, S. Iyer, A. Kumar, L. Li, S. Li, J. Pye, J.F. Torres, B. Wang, Y. Wang, V.M. Wheeler, Progress in heat transfer research for high-temperature solar thermal applications, Appl. Therm. Eng. 184 (2021), 116137, https://doi.org/10.1016/j.applthermaleng.2020.116137.

[7] F. Desai, J. Sunku Prasad, P. Muthukumar, M.M. Rahman, Thermochemical energy storage system for cooling and process heating applications: A review, Energy Convers, Manag. 229 (2021) 113617, https://doi.org/10.1016/j.enconman.2020.113617.

[8] C. Tregambi, M. Troiano, F. Montagnaro, R. Solimene, P. Salatino, Fluidized Beds for Concentrated Solar Thermal Technologies – A Review, Front. Energy Res. 9 (2021), 618421, https://doi.org/10.3389/fenrg.2021.618421.

[9] J.A. Almendros-Ibáñez, M. Fernández-Torrijos, M. Díaz-Heras, J.F. Belmonte, C. Sobrino, A review of solar thermal energy storage in beds of particles: Packed and fluidized beds, Sol. Energy. 192 (2019) 193–237, https://doi.org/10.1016/j.solener.2018.05.047.

[10] M.A. Rivero, D. Rodrigues, C.I.C. Pinheiro, J.P. Cardoso, L.F. Mendes, Solid – gas reactors driven by concentrated solar energy with potential application to calcium looping : A comparative review, Renew. Sustain. Energy Rev. 158 (2022), 112048, https://doi.org/10.1016/j.rser.2021.112048.

[11] C. Tregambi, P. Salatino, R. Solimene, F. Montagnaro, An experimental characterization of Calcium Looping integrated with concentrated solar power, Chem. Eng. J. 331 (2018) 794–802, https://doi.org/10.1016/j.cej.2017.08.068.

[12] R. Chirone, P. Salatino, P. Ammendola, R. Solimene, M. Magaldi, R. Sorrenti, G. De Michele, F. Donatini, Development of a Novel Concept of Solar Receiver/Thermal Energy Storage System Based on Compartmented Dense Gas Fluidized Beds, 14th Int, Conf, Fluid, 2013.

[13] G. Flamant, G. Olalde, High temperature solar gas heating comparison between packed and fluidized bed receivers-I, Sol. Energy. 31 (1983) 463–471, https://doi.org/10.1016/0038-092X(83)90050-6.

[14] N. Gokon, T. Izawa, T. Kodama, Steam gasification of coal cokes by internally circulating fluidized-bed reactor by concentrated Xe-light radiation for solar syngas production, Energy. 79 (2015) 264–272, https://doi.org/10.1016/j.energy.2014.11.012.

[15] X. Li, L. Wei, C.W. Lim, J. Chen, P. Chu, W. Lipiński, N. Yan, Y. Dai, C.-H. Wang, Experimental and numerical study on thermal performance of an indirectly irradiated solar reactor with a clapboard-type internally circulating fluidized bed, Appl. Energy. 305 (2022) 117976, https://doi.org/10.1016/j.apenergy.2021.117976.

[16] X. Li, J. Chen, Q. Hu, P. Chu, Y. Dai, C.H. Wang, Solar-driven gasification in an indirectly-irradiated thermochemical reactor with a clapboard-type internally-circulating fluidized bed, Energy Convers. Manag. 248 (2021), 114795, https://doi.org/10.1016/j.enconman.2021.114795.

[17] M. Díaz-Heras, J.F. Belmonte, J.A. Almendros-Ibáñez, Experimental observations on directly irradiated conical spouted and spout-fluid beds, Exp. Therm. Fluid Sci. 130 (2022), 110488, https://doi.org/10.1016/j.expthermflusci.2021.110488.

[18] M. Díaz-Heras, J.F. Belmonte, J.A. Almendros-Ibáñez, Experimental observations on directly irradiated fluidized beds: Even and uneven fluidization, Exp. Therm. Fluid Sci. 120 (2021), 110242, https://doi.org/10.1016/j.expthermflusci.2020.110242.

[19] C. Tregambi, R. Chirone, F. Montagnaro, P. Salatino, R. Solimene, Heat transfer in directly irradiated fluidized beds, Sol. Energy. 129 (2016) 85–100, https://doi.org/10.1016/j.solener.2016.01.057.

[20] S. Migliozzi, A. Paulillo, R. Chirone, P. Salatino, R. Solimene, Hydrodynamics of compartmented fluidized bed for concentrated solar power and thermnal energy storage applications, Fluid. XV. (2016), https://doi.org/10.1016/j.powtec.2016.12.052.

[21] T. Esence, E. Guillot, M. Tessonneaud, J.L. Sans, G. Flamant, Solar calcination at pilot scale in a continuous flow multistage horizontal fluidized bed, Sol. Energy. 207 (2020) 367–378, https://doi.org/10.1016/j.solener.2020.06.098.

[22] T. Esence, H. Benoit, D. Poncin, M. Tessonneaud, G. Flamant, A shallow cross-flow fluidized-bed solar reactor for continuous calcination processes, Sol. Energy. 196 (2020) 389–398, https://doi.org/10.1016/j.solener.2019.12.029.

[23] J. Gómez-Hernández, P.A. González-Gómez, J.V. Briongos, D. Santana, Technical feasibility analysis of a linear particle solar receiver, Sol. Energy. 195 (2020) 102–113, https://doi.org/10.1016/j.solener.2019.11.052.

[24] C. Tregambi, C. Bevilacqua, M. Troiano, R. Solimene, P. Salatino, A novel autothermal fluidized bed reactor for concentrated solar thermal applications, Chem. Eng. J. 398 (2020), 125702, https://doi.org/10.1016/j.cej.2020.125702.

[25] S. Padula, C. Tregambi, R. Solimene, R. Chirone, M. Troiano, P. Salatino, A novel fluidized bed "thermochemical battery" for energy storage in concentrated solar thermal technologies, Energy Convers. Manag. 236 (2021), 113994, https://doi.org/10.1016/j.enconman.2021.113994.

[26] T. Uchino, C. Fushimi, Fluidized bed reactor for thermochemical heat storage using $Ca(OH)_2$/CaO to absorb the fluctuations of electric power supplied by variable renewable energy sources: A dynamic model, Chem. Eng. J. 419 (2021), 129571, https://doi.org/10.1016/j.cej.2021.129571.

[27] C. Ortiz, J.M. Valverde, R. Chacartegui, L.A. Perez-Maqueda, P. Giménez, The Calcium-Looping ($CaCO_3$/CaO) process for thermochemical energy storage in Concentrating Solar Power plants, Renew. Sustain. Energy Rev. 113 (2019), 109252, https://doi.org/10.1016/j.rser.2019.109252.

[28] E. Darwish, M. Mansouri, D. Yilmaz, H. Leion, Effect of Mn and Cu substitution on the $SrFeO_3$ perovskite for potential thermochemical energy storage applications, Processes. 9 (10) (2021) 1817, https://doi.org/10.3390/pr9101817.

[29] L. André, S. Abanades, Recent Advances in Thermochemical Energy Storage via Solid – Gas Reversible Reactions at High Temperature, Energies 13 (2020) 5859, https://doi.org/10.3390/en13225859.

[30] SOCRATCES (SOlar Calcium-looping integRAtion for ThermoChemical Energy Storage), https://socratces.eu/. Last accessed: February 2022.

[31] CALyPSOL (CALcium oxide LooPing through SOLar energy), https://www.dlr.de/ff/en/desktopdefault.aspx/tabid-18130/28811_read-71705/. Last accessed: May 2022.

[32] M.T. Dunstan, F. Donat, A.H. Bork, C.P. Grey, C.R. Müller, CO_2 Capture at Medium to High Temperature Using Solid Oxide-Based Sorbents: Fundamental Aspects, Mechanistic Insights, and Recent Advances, Chem. Rev. 121 (2021) 12681–12745, https://doi.org/10.1021/acs.chemrev.1c00100.

[33] A. Coppola, O. Senneca, F. Scala, F. Montagnaro, P. Salatino, Looping cycles for low carbon technologies: A survey of recent research activities in Naples, Fuel. 268 (2020), 117371, https://doi.org/10.1016/j.fuel.2020.117371.

[34] C. Tregambi, P. Bareschino, D. Hanak, F. Montagnaro, F. Pepe, E. Mancusi, Modelling of an integrated process for atmospheric carbon dioxide capture and methanation, J. Clean. Prod. 356 (2022), 131827, https://doi.org/10.1016/j.jclepro.2022.131827.

[35] T. Shimizu, T. Hirama, H. Hosoda, K. Kitano, M. Inagaki, K. Tejima, A twin fluid-bed reactor for removal of CO_2 from combustion processes, Chem. Eng. Res. Des. 77 (1999) 62–68, https://doi.org/10.1205/026387699525882.

[36] S. Khosravi, S. Hossainpour, H. Farajollahi, N. Abolzadeh, Integration of a coal fired power plant with calcium looping CO_2 capture and concentrated solar power generation: Energy, exergy and economic analysis, Energy. 240 (2022), 122466, https://doi.org/10.1016/j.energy.2021.122466.

[37] J.P. Rincon Duarte, D. Kriechbaumer, B. Lachmann, S. Tescari, T. Fend, M. Roeb, C. Sattler, Solar calcium looping cycle for CO_2 capturing in a cement plant. Definition of process parameters and reactors selection, Sol. Energy. 238 (2022) 189–202, https://doi.org/10.1016/j.solener.2022.04.031.

[38] U. Tesio, E. Guelpa, V. Verda, Comparison of sCO_2 and He Brayton cycles integration in a Calcium-Looping for Concentrated Solar Power, Energy. 247 (2022), 123467, https://doi.org/10.1016/j.energy.2022.123467.

[39] M. Benitez-Guerrero, B. Sarrion, A. Perejon, P.E. Sanchez-Jimenez, L.A. Perez-Maqueda, J. Manuel Valverde, Large-scale high-temperature solar energy storage using natural minerals, Sol. Energy Mater. Sol. Cells. 168 (2017) 14–21, https://doi.org/10.1016/j.solmat.2017.04.013.

[40] M. Benitez-Guerrero, J.M. Valverde, P.E. Sanchez-Jimenez, A. Perejon, L.A. Perez-Maqueda, Multicycle activity of natural $CaCO_3$ minerals for thermochemical energy storage in Concentrated Solar Power plants, Sol. Energy. 153 (2017) 188–199, https://doi.org/10.1016/j.solener.2017.05.068.

[41] C. Tregambi, F. Di Lauro, F. Montagnaro, P. Salatino, R. Solimene, 110th Anniversary: Calcium Looping Coupled with Concentrated Solar Power for Carbon Capture and Thermochemical Energy Storage, Ind. Eng. Chem. Res. 58 (2019) 21262–21272, https://doi.org/10.1021/acs.iecr.9b03083.

[42] Y. Yang, Y. Li, X. Yan, J. Zhao, C. Zhang, Development of thermochemical heat storage based on CaO/$CaCO_3$ cycles: A review, Energies. 14 (2021) 6847, https://doi.org/10.3390/en14206847.

[43] H. Guo, S. Wang, C. Li, Y. Zhao, Q. Sun, X. Ma, Incorporation of Zr into Calcium Oxide for CO_2 Capture by a Simple and Facile Sol-Gel Method, Ind. Eng. Chem. Res. 55 (2016) 7873–7879, https://doi.org/10.1021/acs.iecr.5b04112.

[44] K.T. Møller, T.D. Humphries, A. Berger, M. Paskevicius, C.E. Buckley, Thermochemical energy storage system development utilising limestone, Chem. Eng. J. Adv. 8 (2021), 100168, https://doi.org/10.1016/j.ceja.2021.100168.

[45] A.N. Antzara, A. Arregi, E. Heracleous, A.A. Lemonidou, In-depth evaluation of a ZrO_2 promoted CaO-based CO_2 sorbent in fluidized bed reactor tests, Chem. Eng. J. 333 (2018) 697–711, https://doi.org/10.1016/j.cej.2017.09.192.

[46] M. Benitez-Guerrero, J.M. Valverde, P.E. Sanchez-Jimenez, A. Perejon, L.A. Perez-Maqueda, Calcium-Looping performance of mechanically modified Al_2O_3-CaO composites for energy storage and CO_2 capture, Chem. Eng. J. 334 (2018) 2343–2355, https://doi.org/10.1016/j.cej.2017.11.183.

[47] A. Antzara, E. Heracleous, A.A. Lemonidou, Improving the stability of synthetic CaO-based CO_2 sorbents by structural promoters, Appl. Energy. 156 (2015) 331–343, https://doi.org/10.1016/j.apenergy.2015.07.026.

[48] M. Heidari, M. Tahmasebpoor, A. Antzaras, A.A. Lemonidou, CO_2 capture and fluidity performance of CaO-based sorbents: Effect of Zr, Al and Ce additives in tri-, bi- and mono-metallic configurations, Process Saf. Environ. Prot. 144 (2020) 349–365, https://doi.org/10.1016/j.psep.2020.07.041.

[49] D. Choi, A.-H. Alissa Park, Y. Park, Effects of eutectic alkali chloride salts on the carbonation reaction of CaO-based composites for potential application to a thermochemical energy storage system, Chem. Eng. J. 437 (2022), 135481, https://doi.org/10.1016/j.cej.2022.135481.
[50] M. Sayyah, Y. Lu, R.I. Masel, K.S. Suslick, Mechanical Activation of CaO-Based Adsorbents for CO_2 Capture, ChemSusChem. 6 (2013) 193–198, https://doi.org/10.1002/cssc.201200454.
[51] M. Benitez-Guerrero, J.M. Valverde, A. Perejon, P.E. Sanchez-Jimenez, L.A. Perez-Maqueda, Effect of milling mechanism on the CO_2 capture performance of limestone in the Calcium Looping process, Chem. Eng. J. 346 (2018) 549–556, https://doi.org/10.1016/j.cej.2018.03.146.
[52] F. Di Lauro, C. Tregambi, F. Montagnaro, P. Salatino, R. Chirone, R. Solimene, Improving the performance of calcium looping for solar thermochemical energy storage and CO_2 capture, Fuel. 298 (2021), 120791, https://doi.org/10.1016/j.fuel.2021.120791.
[53] J.M. Valverde, M. Barea-López, A. Perejón, P.E. Sánchez-Jiménez, L.A. Pérez-Maqueda, Effect of Thermal Pretreatment and Nanosilica Addition on Limestone Performance at Calcium-Looping Conditions for Thermochemical Energy Storage of Concentrated Solar Power, Energy and Fuels. 31 (2017) 4226–4236, https://doi.org/10.1021/acs.energyfuels.6b03364.
[54] J. Arcenegui-Troya, P.E. Sánchez-Jiménez, A. Perejón, V. Moreno, J.M. Valverde, L.A. Pérez-Maqueda, Kinetics and cyclability of limestone ($CaCO_3$) in presence of steam during calcination in the CaL scheme for thermochemical energy storage, Chem. Eng. J. 417 (2021) 129194, https://doi.org/10.1016/j.cej.2021.129194.
[55] J. Arcenegui-Troya, P.E. Sánchez-Jiménez, A. Perejón, J.M. Valverde, L.A. Pérez-Maqueda, Steam-enhanced calcium-looping performance of limestone for thermochemical energy storage: The role of particle size, J. Energy Storage. 51 (2022) 104305, https://doi.org/10.1016/j.est.2022.104305.
[56] A. Coppola, A. Esposito, F. Montagnaro, G. De Tommaso, F. Scala, P. Salatino, Effect of exposure to SO_2 and H_2O during the carbonation stage of fluidised bed calcium looping on the performance of sorbents of different nature, Chem. Eng. J. 377 (2019), 120626, https://doi.org/10.1016/j.cej.2018.12.086.
[57] L. Yang, G. Huang, Z. Huang, Optimized design of Ca-based thermochemical heat storage materials for concentrated solar power, J. Energy Storage. 43 (2021), 103236, https://doi.org/10.1016/j.est.2021.103236.
[58] H. Zheng, X. Liu, Y. Xuan, C. Song, D. Liu, Q. Zhu, Z. Zhu, K. Gao, Y. Li, Y. Ding, Thermochemical heat storage performances of fluidized black $CaCO_3$ pellets under direct concentrated solar irradiation, Renew. Energy. 178 (2021) 1353–1369, https://doi.org/10.1016/j.renene.2021.07.026.
[59] Y. Da, Y. Xuan, L. Teng, K. Zhang, X. Liu, Y. Ding, Calcium-based composites for direct solar-thermal conversion and thermochemical energy storage, Chem. Eng. J. 382 (2020), 122815, https://doi.org/10.1016/j.cej.2019.122815.
[60] V. Moreno, J. Arcenegui-Troya, P. Enrique Sánchez-Jiménez, A. Perejón, R. Chacartegui, J. Manuel Valverde, L. Allan Pérez-Maqueda, Albero: An alternative natural material for solar energy storage by the calcium-looping process, Chem. Eng. J. 440 (2022), 135707, https://doi.org/10.1016/j.cej.2022.135707.
[61] A. Scaltsoyiannes, A. Antzaras, G. Koilaridis, A. Lemonidou, Towards a generalized carbonation kinetic model for CaO-based materials using a modified random pore model, Chem. Eng. J. 407 (2021), 127207, https://doi.org/10.1016/j.cej.2020.127207.
[62] G.M. Castilla, D.C. Guío-Pérez, S. Papadokonstantakis, F. Johnsson, D. Pallarès, Techno-economic assessment of calcium looping for thermochemical energy storage with CO_2 capture, Energies. 14 (2021) 1–17, https://doi.org/10.3390/en14113211.
[63] B. Sarrion, J.M. Valverde, A. Perejon, L. Perez-Maqueda, P.E. Sanchez-Jimenez, On the Multicycle Activity of Natural Limestone/Dolomite for Thermochemical Energy Storage of Concentrated Solar Power, Energy Technol. 4 (2016) 1013–1019, https://doi.org/10.1002/ente.201600068.
[64] B. Sarrión, A. Perejón, P.E. Sánchez-Jiménez, L.A. Pérez-Maqueda, J.M. Valverde, Role of calcium looping conditions on the performance of natural and synthetic Ca-based materials for energy storage, J. CO2 Util. 28 (2018) 374–384, https://doi.org/10.1016/j.jcou.2018.10.018.
[65] S. Pascual, P. Lisbona, M. Bailera, L.M. Romeo, Design and operational performance maps of calcium looping thermochemical energy storage for concentrating solar power plants, Energy. 220 (2021), 119715, https://doi.org/10.1016/j.energy.2020.119715.
[66] S. Pascual, P. Lisbona, L.M. Romeo, Operation maps in calcium looping thermochemical energy storage for concentrating solar power plants, J. Energy Storage. 55 (2022), 105771, https://doi.org/10.1016/j.est.2022.105771.
[67] C. Tregambi, P. Bareschino, E. Mancusi, F. Pepe, F. Montagnaro, R. Solimene, P. Salatino, Modelling of a concentrated solar power – photovoltaics hybrid plant for carbon dioxide capture and utilization via calcium looping and methanation, Energy Convers. Manag. 230 (2021), 113792, https://doi.org/10.1016/j.enconman.2020.113792.
[68] L.M. Romeo, Y. Lara, P. Lisbona, J.M. Escosa, Optimizing make-up flow in a CO_2 capture system using CaO, Chem. Eng. J. 147 (2009) 252–258, https://doi.org/10.1016/j.cej.2008.07.010.
[69] G.S. Grasa, J.C. Abanades, CO_2 Capture Capacity of CaO in Long Series of Carbonation/Calcination Cycles, Ind. Eng. Chem. Res. 45 (2006) 8846–8851, https://doi.org/10.1021/ie0606946.
[70] G. Olivieri, A. Marzocchella, P. Salatino, A fluid-bed continuous classifier of polydisperse granular solids, J. Taiwan Inst. Chem. Eng. 40 (2009) 638–644, https://doi.org/10.1016/j.jtice.2009.05.011.
[71] G. Olivieri, A. Marzocchella, P. Salatino, Segregation of fluidized binary mixtures of granular solids, AIChE J. 50 (2004) 3095–3106, https://doi.org/10.1002/aic.10340.
[72] J.R. Grace, Fluidized-bed hydrodynamics, in: G. Hetsroni (Ed.), Handb. Multiph. Syst., Washington: Hemisphere, 1982: pp. 8–1-8–64.
[73] C. Tregambi, R. Solimene, F. Montagnaro, P. Salatino, M. Marroccoli, N. Ibris, A. Telesca, Solar-driven production of lime for ordinary Portland cement formulation, Sol. Energy. 173 (2018) 759–768, https://doi.org/10.1016/j.solener.2018.08.018.
[74] S. Telschow, F. Frandsen, K. Theisen, K. Dam-Johansen, Cement formation-A success story in a black box: High temperature phase formation of portland cement clinker, Ind. Eng. Chem. Res. 51 (2012) 10983–11004, https://doi.org/10.1021/ie300674j.
[75] M. Alonso, Y. Álvarez Criado, J.R. Fernández, C. Abanades, CO_2 Carrying Capacities of Cement Raw Meals in Calcium Looping Systems, Energy and Fuels. 31 (2017) 13955–13962, https://doi.org/10.1021/acs.energyfuels.7b02586.
[76] M. Alonso, J.R. Fernández, J.C. Abanades, Kinetic Study of Belite Formation in Cement Raw Meals Used in the Calcium Looping CO_2 Capture Process, Ind. Eng. Chem. Res. 58 (2019) 5445–5454, https://doi.org/10.1021/acs.iecr.9b00813.
[77] J.M. Valverde, A. Perejon, L.A. Perez-Maqueda, Enhancement of fast CO_2 capture by a nano-SiO_2/CaO composite at Ca-looping conditions, Environ. Sci. Technol. 46 (2012) 6401–6408, https://doi.org/10.1021/es3002426.
[78] R. Barker, The reversibility of the reaction $CaCO_3 \rightleftarrows CaO+CO_2$, J. Appl. Chem. Biotechnol. 23 (1973) 733–742, https://doi.org/10.1002/jctb.5020231005.
[79] M. Tawfik, A review of directly irradiated solid particle receivers: Technologies and influencing parameters, Renew. Sustain. Energy Rev. 167 (2022), 112682, https://doi.org/10.1016/j.rser.2022.112682.
[80] C.K. Ho, A review of high-temperature particle receivers for concentrating solar power, Appl. Therm. Eng. 109 (2016) 958–969, https://doi.org/10.1016/j.applthermaleng.2016.04.103.
[81] A. Telesca, M. Marroccoli, M. Tomasulo, G.L. Valenti, H. Dieter, F. Montagnaro, Calcium looping spent sorbent as a limestone replacement in the manufacture of portland and calcium sulfoaluminate cements, Environ. Sci. Technol. 49 (2015) 6865–6871, https://doi.org/10.1021/acs.est.5b00394.
[82] A. Telesca, D. Calabrese, M. Marroccoli, M. Tomasulo, G.L. Valenti, G. Duelli (Varela), F. Montagnaro, Spent limestone sorbent from calcium looping cycle as a raw material for the cement industry, Fuel. 118 (2014) 202–205, https://doi.org/10.1016/j.fuel.2013.10.060.